Eur. J. Mineral.
2006, **18**, 149–160

Slip systems and plastic shear anisotropy in Mg_2SiO_4 ringwoodite: insights from numerical modelling

PHILIPPE CARREZ[1,*], PATRICK CORDIER[1], DAVID MAINPRICE[2] and ANDREA TOMMASI[2]

[1]Laboratoire de Structure et Propriétés de l'Etat Solide – UMR CNRS 8008, Université des Sciences et Technologies de Lille, Cité Scientifique, Bat C6, F-59655 Villeneuve d'Ascq, France
*Corresponding author, e-mail: philippe.carrez@univ-lille1.fr
[2]Laboratoire de Tectonophysique, UMR CNRS 5568, Université de Montpellier II, F-34095 Montpellier cedex 5, France

Abstract: Knowledge on the deformation mechanisms of Mg_2SiO_4 ringwoodite is important for the understanding of flow and seismic anisotropy in the Earth's mantle transition zone. We report here the first numerical modelling of dislocation structures in ringwoodite. The dislocation properties are calculated through the Peierls-Nabarro model using the generalized stacking fault (GSF) results as a starting model. The GSF are determined from first-principle calculations using the code VASP. They enable us to determine the relative ease of slip for dislocation glide systems in ringwoodite. The dislocation properties such as core spreading and Peierls stresses were determined for the easy dislocation glide systems. Our results show that ½<110>{110} and ½<110>{111} are the easiest slip systems in ringwoodite at 20 GPa and 0 K. These results are used as input of a viscoplastic model to predict the deformation of a ringwoodite rich aggregate. Calculated crystal preferred orientation (CPO) accounts satisfactorily for experimental data available from either diamond anvil cell or D-DIA experiments.

Key-words: ringwoodite, deformation mechanisms, dislocations, slip systems, first-principle calculations, Peierls-Nabarro model, seismic anisotropy, Earth mantle transition zone.

1. Introduction

$(Mg,Fe)_2SiO_4$ ringwoodite is a high-pressure polymorph of olivine with a spinel structure. It is widely considered to be the most abundant phase in the lower half of the mantle transition zone in the depth range 550–670 km (Irifune & Ringwood, 1987). Understanding crystal defects and plasticity of ringwoodite is thus critical for modelling the dynamics of the interior of the Earth. Information on defects in ringwoodite have first been obtained from the microstructural study of shocked chondrite meteorites. Madon & Poirier (1983) have reported evidence for ½<110>{111} dislocation slip from observations of the Tenham meteorite. ¼<110>{110} stacking faults have also been reported in numerous cases (Putnis & Price, 1979; Vaughan & Kohlstedt, 1981; Madon & Poirier, 1983; Rubie & Brearley, 1990, 1994) but they are usually interpreted as resulting from phase transformations and do not seem to be related to plasticity.

Conducting plastic deformation experiments in P, T conditions of the deep Earth is still one of the most important challenges for mineral physics. The newly developed deformation experiments dedicated to high-pressure (Deformation-DIA, Wang *et al.*, 2003; and Rotational Drickamer Apparatus, Yamasaki & Karato, 2001) cannot reach the P, T conditions prevailing in the lower part of the transition zone. Above 15 GPa, deformation experiments must be undertaken with a multianvil apparatus (*e.g.* Cordier & Rubie, 2001; Cordier *et al.*, 2004) or with a diamond anvil cell (*e.g.* Wenk *et al.*, 2004). The first deformation experiment on $(Mg,Fe)_2SiO_4$ ringwoodite has been performed by Karato *et al.* (1998) at 16 GPa and 1600 K using a shear deformation assembly in a multianvil apparatus. Two slip systems have been identified by transmission electron microscopy: ½<110>{111} and ½<110>{100}. In contrast, a more recent study of Mg_2SiO_4 ringwoodite samples deformed at 22 GPa between 1400 and 1500°C (Thurel, 2001) has revealed evidence for slip on ½<110>{111} and on ½<110>{110}. Flow laws for ringwoodite at subduction zone conditions (20 GPa, T < 1350°C) have been obtained recently by Xu *et al.* (2003) using a T-cup multianvil apparatus with in situ measurements based on synchrotron-generated X-rays but no microstructural investigations were conducted on these samples. Room-temperature deformation of ringwoodite has been achieved using diamond anvil cells (Kavner & Duffy, 2001; Wenk *et al.*, 2004). Ringwoodite transformed *in situ* from San Carlos olivine is shown to develop weak preferred orientations with {110} lattice planes perpendicular to the compression direction (Wenk *et al.*, 2004). Recently, room-temperature deformation experiments have been performed on Mg_2SiO_4 ringwoodite using the D-DIA (Nishiyama *et al.*, 2005; Wenk *et al.*, 2005) where stress-strain curves could be measured *in*

DOI: 10.1127/0935-1221/2006/0018-0149
0935-1221/06/0018-0149 $ 5.40

situ at high pressures. These studies, based on *in situ* crystal preferred orientation measurements, emphasize that slip on ½<110>{111} dominates deformation under those conditions.

Computational materials science is an alternative approach to study plastic deformation. The Peierls-Nabarro (PN) model provides a conceptual framework for addressing the issue of dislocation structures (Hirth & Lothe, 1982). The model is essentially based on continuum mechanics (far from the defect), but inelastic displacements in the dislocation core are given a specific description. A recent approach for describing forces in the dislocation core is based on the concept of generalized stacking fault (GSF) surfaces (Vitek, 1968; Christian & Vitek, 1970). The value of the GSF is obtained by shearing half of the infinite crystal over the other half. The fault is called „generalized" because it is unstable for most values of shear and must be balanced by a restoring force (which is introduced in the PN model). The GSF can nowadays be calculated accurately from first-principles. The GSF gives access to the ideal shear strength which is the upper bound on the mechanical strength of a solid. This approach has been applied to many metallic systems: Al (Paxton *et al.*, 1991; Hartford *et al.* 1998; Roundy *et al.*, 1999; Ogata *et al.*, 2002), Cu (Roundy *et al.*, 1999; Ogata *et al.*, 2002), Pd (Hartford *et al.* 1998), Fe (Clatterbuck *et al.*, 2002), Mo (Xu & Moriarty, 1996; Luo *et al.* 2002), Nb (Luo *et al.*, 2002), W (Krenn *et al.*, 2001; Roundy *et al.*, 2001), Ta (Söderlind & Moriarty, 1998) and Zr (Domain *et al.*, 2004). Recently we have calculated GSF for forsterite (Durinck *et al.*, 2005) and shown that, despite a complex crystal chemistry, this approach could account for plastic anisotropy in this mineral. It is thus possible to build more realistic models of dislocations using a PN model in which the inelastic displacements in the dislocation core are described using the GSF approach. Several examples are available in the recent literature: Al (Sun & Kaxiras, 1997; Hartford *et al.*, 1998), Pd (Hartford *et al.*, 1998), NiAl and FeAl (Medvedeva *et al.*, 1996), TiAl and CuAu (Mryasov *et al.*, 1998), Si (Kaxiras & Duesbery, 1993; Joos *et al.*, 1994; de Koning *et al.*, 1998) and MgO (Miranda & Scandolo, 2005).

In the present study, we use the GSF framework to assess plastic strain anisotropy of ringwoodite at the atomic scale from first-principle calculations. Dislocation properties are derived from GSF through the Peierls-Nabarro (PN) model. This approach is combined with elasticity to infer the possible slip systems in ringwoodite. Self-consistent viscoplastic models are finally used to evaluate the crystal-preferred orientation that will result from the activation of these slip systems and compare our results with ringwoodite crystal preferred orientations produced in recent low-temperature deformation experiments.

2. Crystallography of slip in the spinel structure

Ringwoodite exhibits a spinel structure based on a face-centred-cubic packing of the oxygen sublattice. Silicon atoms are located in the tetrahedral sites whereas octahedral sites are occupied by magnesium and iron atoms. The space group of Mg_2SiO_4 is *Fd3m* and the lattice parameter is

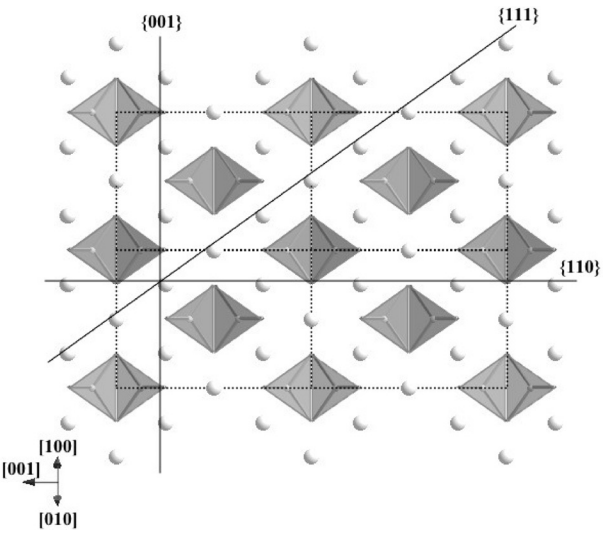

Fig. 1. Ringwoodite structure viewed along <110> with potential slip planes. The unit cells are shown in dashed lines.

8.071 Å (Ringwood & Major,1970). The slip direction in spinel is always observed to be parallel to the shortest lattice vector of the fcc oxygen lattice: ½<110>. The observed slip plane is variable. The most commonly observed slip planes are {111} and {110}, although {100} have been reported in magnetite, nickel ferrite and chromite (see a detailed review in Mitchell, 1999). Figure 1 shows the structure of ringwoodite viewed along <110>. The planes usually reported as slip planes in the spinel structure are indeed potential slip planes for ringwoodite as they do not require breaking the strong Si-O bonds. In oxides with spinel structures, dislocations are generally observed to be dissociated into collinear partials following the reaction: ½<110> → ¼<110> + ¼<110>. The dissociation width increase with increasing deviation from stoichiometry, implying that the stacking fault energy decrease (between 180 and 20 mJ/m^2, Mitchell, 1999). A variety of dissociation planes have been reported: {111}, {110}, {100}, and {311}.

3. Computational procedures

3.a Ab initio calculations

Calculations were performed using the *ab initio* total-energy calculation package VASP (Vienna Ab Initio Package) developed by Kresse and Hafner (Kresse & Hafner, 1993, 1994; Kresse & Furthmüller, 1996a). This code is based on the first-principles density functional theory and solves the effective one-electron Hamiltonian involving a functional of the electron density to describe the exchange-correlation potential. It gives access to the total energy of a periodic system with as a single input the atomic numbers of atoms. Computational efficiency is achieved using a plane wave basis set for the expansion of the single electron wave functions and fast numerical algorithms to perform self-consistent calculations (Kresse & Furthmüller, 1996b). Within this scheme, we used the Generalised Gradient Approximation (GGA) derived by Perdrew & Wang (1992) and ultrasoft

pseudopotentials (*e.g.* Vanderbilt, 1990 or Kresse & Hafner, 1994). Using this assumption, the outmost core radius for the Mg, Si and O atoms are 1.058, 0.953 and 0.820 Å respectively. Computation convergence better than 4.10^{-5} eV/atom is achieved in all simulations by using a single energy cut-off value of 600 eV for the plane wave expansion. The first Brillouin zone is sampled using a Monkhorst-Pack grid (Monkhorst & Pack, 1976) adapted for each supercell geometry in order to achieve the full energy convergence. As an example, ringwoodite unit cell calculations were performed using a 4x4x4 grid with a convergence energy less than 0.25 meV for all external pressure conditions.

The ringwoodite crystallographic structure was optimised (full relaxation of the cell parameters and of the atomic positions within the cell) for pressure conditions ranging from 0 to 32 GPa. To determine the athermal elastic constants of the cubic cell, we strained the equilibrium cell using adapted deformations, which were kept lower than 2%. To account for the pressure effect, the calculations of the elastic constants were performed along the lines described by Barron & Klein (1965). As an illustration, c_{11} can be obtained by applying a strain $e_{11} = e$ to the pressurized cell. The associated elastic energy variation is then:

$$\frac{\Delta E}{V} = -pe + \frac{1}{2}c_{11}\,e^2 \qquad (1)$$

where p is the confining pressure.

For c_{44} determination, we can apply a strain $e_{12} = e$ and deduce c_{44} from

$$\frac{\Delta E}{V} = 2c_{44}\,e^2 \qquad (2)$$

c_{12} can be determined by applying $e_{11} = e_{22} = e$ which leads to

$$\frac{\Delta E}{V} = -2pe + (c_{11} + c_{12} - p)e^2 \qquad (3)$$

The elastic constants are then determined from the fit of the total energy versus strain by a second order polynomial.

Calculating a GSF for a given slip system requires a supercell with an adapted geometry. The supercell is built on a Cartesian reference frame defined by the normal to the stacking fault plane (located in the middle of the supercell) and by the shear direction. All our supercells contain a Burgers vector of the spinel structure, ½<110>, which is the shortest lattice repeat along that direction. The last direction is then defined as the cross product of the two previous. Despite the fact that ringwoodite has a cubic structure, we decided to build the supercell with only one stacking fault and it was necessary to add a vacuum buffer parallel to the stacking plane. In this way, the number of atoms in the supercell was reduced compared to the symmetric construction with two stacking fault. It is shown that a thickness of 6 Å of the buffer vacuum and five atomic layers on both sides of the stacking fault are sufficient to guarantee energy accuracy better than 0.01 % with a 2x2x2 Monkhorst-Pack grid. The GSF are then calculated by imposing a given shear displacement value to the upper part of the supercell.

For calculations of relaxed GSF, we tried to allow the maximum number of degrees of freedoms for the atoms without performing full relaxations calculations. The supercell vectors are kept fixed at the values obtained for a bulk system submitted to the pressure of interest. Atoms present on the two surfaces are maintained fixed to mimic the action of the surrounding bulk atoms in the direction normal to the shear plane. Using these conditions, we preserve pressure and shear mostly by imposing conditions on silicon atoms which are only allowed to accommodate shear perpendicularly to the slip plane. Finally, the remaining atoms are fully relaxed in the three directions to account for structural degrees of freedom associated to the crystal chemistry.

3.b Polycrystalline plasticity models

Development of crystal preferred orientations (CPO) in ringwoodite polycrystals deformed in simple shear under high-pressure conditions is simulated using a viscoplastic self-consistent (VPSC) model (Molinari *et al.*, 1987; Lebensohn & Tomé, 1993). In this model, as in all polycrystal plasticity approaches, CPO evolution is essentially controlled by the imposed deformation, the initial texture, and the active slip systems. The latter depend on the mineral structure, but also on the temperature and pressure conditions, which control their relative strength or critical resolved shear stress (CRSS). Extensive testing on metallic alloys (Lebensohn & Tomé, 1993; Logé *et al.*, 2000), halite (Lebensohn *et al.*, 2003), and garnet (Mainprice *et al.*, 2004) as well as on highly anisotropic minerals, such as calcite (Tomé *et al.*, 1991), olivine (Wenk *et al.*, 1991; Tommasi *et al.*, 2000), clinopyroxene (Bascou *et al.*, 2002), and wadsleyite (Tommasi *et al.*, 2004) show that this model produces robust CPO predictions. Detailed information about the calculation procedure can be found in Tomé & Canova (2000).

In the present study, we investigate the evolution of ringwoodite CPO for two end-member deformation regimes: simple shear and axial shortening. Actual flow in the transition zone is most likely three-dimensional, but regions submitted to large deformations probably display a strong shear component, whose orientation (horizontal or steeply dipping) will depend on the large-scale convection pattern. Moreover, CPO obtained in axial shortening simulations can be compared to ringwoodite CPO measured during compression experiments at high pressure (Wenk *et al.*, 2004, Wenk *et al.*, 2005). The only tuning parameters are the active slip systems for ringwoodite, their CRSS and stress exponent. The CRSS for the various slip systems in ringwoodite are inferred from the Peierls stress analysis (see below). Hardening is not considered in the present models, because there are no constraints on the hardening behavior of ringwoodite. Moreover the high temperatures prevailing at transition zone conditions should allow for easy recovery. The actual stress exponent for ringwoodite is unknown, however, oxide spinels are usually characterized by n = 4 (whatever the stoichiometry, see Mitchell, 1999). Simulations were thus run for n = 3 to 5. Indeed, VPSC simulations are not very sensitive to variations of n values within this range; increasing n enhances the plastic anisotropy and hence slightly accelerates the CPO evolution.

4. Elasticity

4.a Elastic constants

We have calculated the anisotropic athermal elastic constants c_{ij} up to 32 GPa. The results are presented in Fig. 2. In general, the elastic constants increase linearly with increasing pressure. The slope is more pronounced for c_{11} compared to c_{12} and c_{44}. The anisotropy factor for cubic symmetry crystals $A = 2c_{44}/(c_{11} - c_{12})$ decreases from 1.24 to 1.11 when pressure increases from 0 to 20 GPa. The elastic anisotropy of ringwoodite is thus small with nearly no anisotropy effect at typical pressure conditions of the transition zone (around 20 GPa). The Cauchy relation, $c_{12} - c_{44} = 2P$ is valid only when all interatomic forces are central. As pressure increases, the calculated values of $c_{12} - c_{44} - 2P$ decrease to reach –13 GPa at 20 GPa and –3 GPa at 30 GPa. This indicates that bonding in ringwoodite exhibits a more ionic character as pressure increases.

Figure 2 shows that our calculated elastic constants compare well with experimental data from Sinogeikin *et al.* (2001) and with Local Density Approximation (LDA) calculations from Kiefer *et al.* (1997). Our results are systematically below Sinogeikin *et al.*'s, as expected from GGA calculations which are known to generally overestimate the unit cell volume and induce under binding. The unit cell parameter determined in this study is 8.13 Å at 0 GPa which is indeed higher than the experimental value of 8.07 Å measured at 300 K by Ringwood & Major (1970) or Meng *et al.* (1994). Conversely, elastic constants calculated using LDA approach by Kiefer *et al.* (1997), are higher than the experimental results.

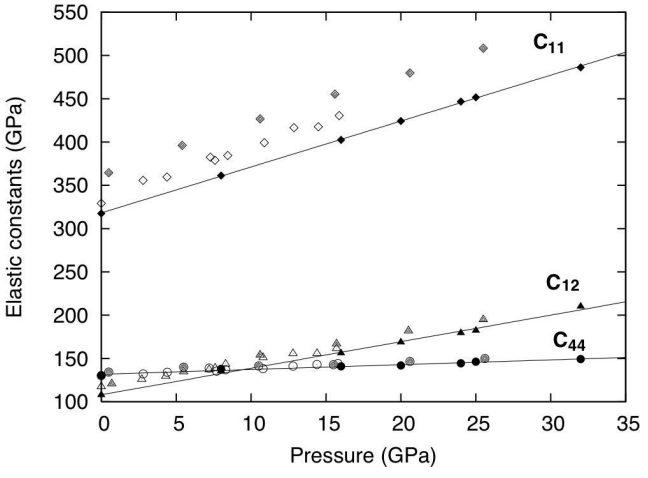

Fig. 2. Elastic constants evolution in function of pressure. (Diamonds = C_{11}, triangles = C_{12} and circles = C_{44}). Results of our GGA calculations (filled symbols) are compared to experimental data (open symbols) from Sinogeikin *et al.* (2001) and to LDA results (grey symbols) from Kieffer *et al.* (1997).

4.b Dislocation line energy

The elastic energy E_{el} per unit length of a straight dislocation is given by:

$$E_{el} = \frac{K(\theta)b^2}{4\pi} ln\left(\frac{R}{r_0}\right) \quad (4)$$

where $K(\theta)$, the energy coefficient is function of the dislocation character which is defined by the angle (θ) between the line direction and the Burgers vector, b is the Burgers vector, and r_0 and R are the integration boundary limits (Hirth & Lothe, 1982). For an isotropic crystal, $K(\theta)$ is

$$K(\theta) = \mu\left(\frac{sin^2\theta}{1-\upsilon} + cos^2\theta\right) \quad (5)$$

where μ is the shear modulus and υ the Poisson ratio. The main effect of elastic anisotropy on the dislocation line energy is found in the energy coefficient K which can be calculated within the frame of the Stroh theory (Hirth & Lothe, 1982). The DisDi software (Douin, 1987; Douin *et al.*, 1986) is based on this theory. It has been used here to calculate the energy coefficients $K(\theta)$ and the dislocation line energies. The dislocation line energies predicted using elastic constants calculated at 20 GPa are presented on Fig. 3 for several slip systems: those corresponding to ½<110> slip in the three planes {100}, {110} and {111} as well as two slip systems corresponding to <100> slip in {011} and {001} planes. Using experimental values for the elastic constants or changing the pressure has no significant influence on the result. Slip along <100> appears clearly less favourable from the energetic point of view with a line energy twice as large as those corresponding to ½<110> slip. Figure 3 confirms that the effects of elastic anisotropy are very small:

– the ratio between the line energies of edge and screw dislocations varies from 1.37 and 1.40 for ½<110> depending on the glide plane, which is very close from the value derived from the isotropic case $1/(1-\upsilon) \approx 1.4$
– the line energy of a ½<110> dislocation is almost independent of the choice of slip plane

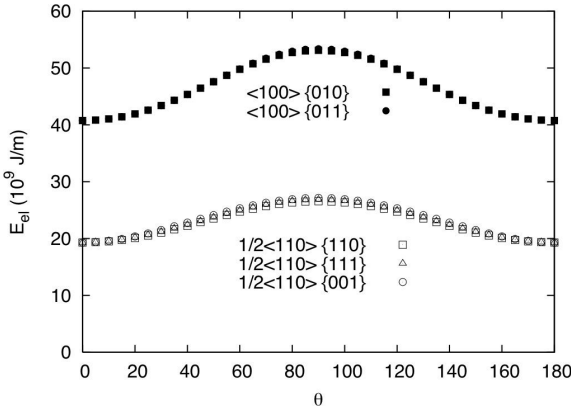

Fig. 3. Dislocation line energies for several potential slip systems (elastic constants from our calculations at 20 GPa).

5. Plastic shear

5.a Generalized Stacking Faults (GSF)

The GSF excess energies γ have been calculated for several shear configurations. Three of them correspond to the slip

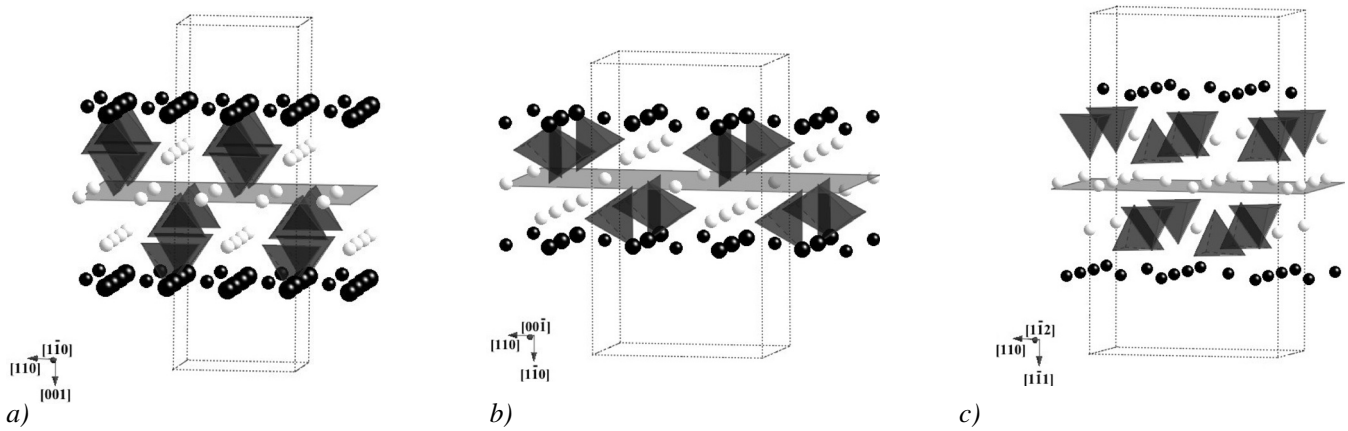

a) *b)* *c)*

Fig. 4. Unsheared supercells of various GSF calculations. The shear planes are presented in light grey. SiO_4 tetrahedra are displayed in dark grey, white atoms corresponding to Mg. Atoms in dark at surfaces are either O or Mg fixed. The supercells are used to calculate the GSF associated with the following slip systems:
a) ½<110>{001}; b) ½<110>{011}, <100>{011}; c) ½<110>{111}.

systems commonly reported in the spinel structure, ½<110>{001}, ½<110>{110} and ½<110>{111}, as discussed in section 2. Possible shear along <100> on {001} and {001} has also been considered. The supercell constructed for the GSF calculations are presented on Fig. 4. Following the results of Durinck *et al.* (2005), the fault level (in the middle of the supercell) is chosen so as not to cut the strong SiO_4 structural units. In case of shear on {001}, two cutting levels could be considered: one in the Mg layer and one between the SiO_4 tetrahedra. We have chosen to shear the structure along the Mg layer which corresponds to the largest interplanar distance.

The unrelaxed GSF are presented on Fig. 5. The energy is determined for several shear values S between 0 and b without any relaxation of the atomic position. It is shown that <100> slip is very unfavourable due to strong impingement of magnesium and oxygen atoms (Fig. 5). The three barriers associated with ½<110> slip are very similar with a camel-hump shape. The only significant difference lies in the 50 % shear excess energy which is higher for slip on {001}.

More realistic values can be obtained by allowing atomic relaxations at each shear step. We tried to leave the atoms as free as possible in their displacements. Shear has to be imposed however. This is achieved by using the boundary conditions and the atomic relaxation scheme defined in section 3. The excess energy barriers at 0 GPa after relaxation are presented on Fig. 6. As expected, atomic relaxations result in a significant decrease of the GSF energies. However, the barriers keep their shapes. This is important as a camel-hump barrier suggest the possibility of a core extension within the plane with potential implications for dislocation mobility as discussed later. It is interesting to note that the three barriers shown on Fig. 6 are clearly distinct after relaxation. This shows that the relaxation mechanisms are very sensitive to the actual atomic environments at the shear plane. The highest energy barrier is associated with ½<110>{001}, whereas ½<110>{110} corresponds to the lowest (see Table 1). It is difficult however to infer the relative resistance to plastic shear simply by looking at the energy barriers. The simplest approach consists in calculating the shear resistance from the derivative of the GSF (Vítek, 1974; Medvedeva *et al.*, 1996; Sun & Kaxiras, 1997; Hartford *et al.*, 1998), which gives access to the restoring force:

$$\overrightarrow{F}(S) = -\overrightarrow{grad}\gamma(S) \qquad (6)$$

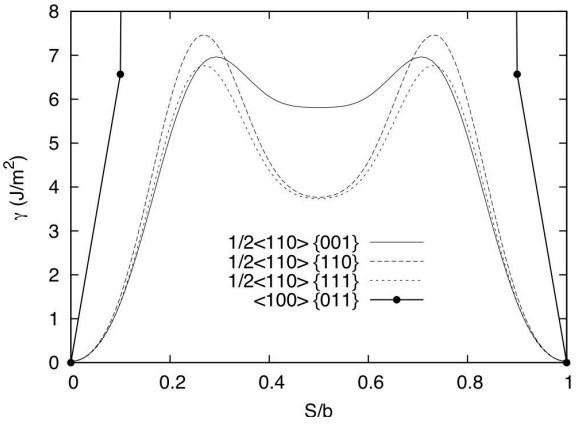

Fig. 5. Unrelaxed generalized stacking fault excess energies γ as a function of displacement shear S (expressed as a fraction of the modulus of the Burgers vector ½ <110>). Pressure: 0 GPa.

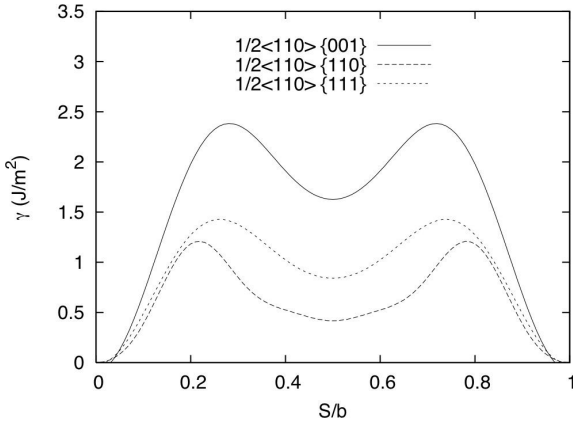

Fig. 6. Influence of atomic relaxations on the GSF at 0 GPa.

Table 1. Parameters issued from the GSF calculations. γ^{max} is the maximum value of the excess energy barrier. τ^{max} is the ideal shear stress. In the last column, the ISS are normalised by the anisotropic shear moduli calculated from anisotropic elasticity. All values are presented at 0 and 20 GPa.

Pressure (GPa)	Slip plane	b (Å)	$\mu_{<uvw>\{hkl\}}$ (GPa)	γ^{max} (J/m^2)	τ^{max} (GPa)	$\tau^{max}/\mu_{<uvw>\{hkl\}}$
0	{001}	5.75	131	2.4	24	0.19
	{110}		105	1.2	17	0.16
	{111}		112	1.4	15	0.13
20	{001}	5.57	142	3.3	44	0.31
	{110}		128	2.1	26	0.20
	{111}		132	2.3	25	0.19

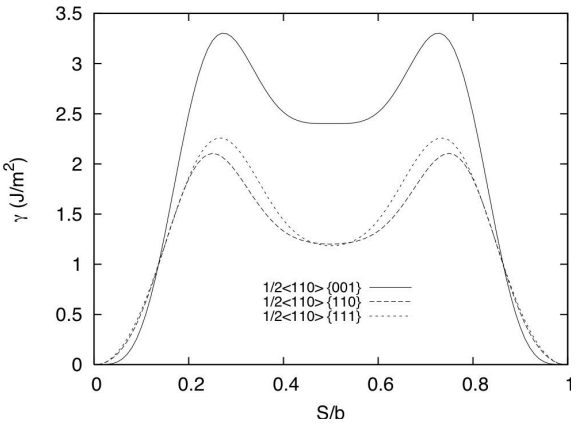

Fig. 7. Relaxed GSF at 20 GPa.

The ideal shear strength (ISS) which is defined as the „maximum resolved shear stress that an ideal, perfect crystal can suffer without plastically deforming" (Paxton *et al.*, 1991) is identified to the maximum stress τ^{max} along the shear displacement. The values of τ^{max} are presented in Table 1. The resistance to plastic shear is very comparable on {110} and on {111} (the maximum of the slope is found at the beginning of the curve which governs the value of the ISS). Normalizing τ^{max} by the shear modulus enables comparison with other structures. Most metals yield values in the range 0.09–0.17 μ (Paxton *et al.*, 1991; Söderlind *et al.*, 1998; Roundy *et al.*, 1999; Krenn *et al.*, 2001) which compare very well with our values for the easiest slip planes {111} and {110}.

The influence of pressure on plastic shear of ringwoodite is presented on Fig. 7 which shows the relaxed GSF at 20 GPa, a pressure representative of the lower part of the transition zone where ringwoodite is stable. For this purpose, a new reference state is obtained under pressure, which is then sheared. Atoms present at the interface with the vacuum layer (shown in black on Fig. 4) must obviously be fixed. As expected, pressure makes ringwoodite stronger. The influence of pressure on plastic deformation can have two origins however. One is due to the evolution with pressure of the elastic constants. The increase with pressure of the normalized ISS presented in Table 1 demonstrates that the elastic contribution is not the only one. The atomic configuration in the shear plane also plays an important role. The energy barriers of Fig. 7 and the ISS presented in Table 1 suggest that homogeneous plastic shear at 20 GPa is easier in {110} and {111}. The two planes exhibit very comparable behaviours.

5.b From GSF to dislocations using the Peierls-Nabarro model

The Peierls-Nabarro model assumes that the misfit region of inelastic displacement is restricted to the glide plane, whereas linear elasticity applies far from it. The dislocation corresponds to a continuous distribution of shear $S(x)$ along the glide plane (x is the coordinate normal to the dislocation line in the glide plane). $S(x)$ represents the disregistry across the glide plane. The stress generated by the shear displacement $S(x)$ can be represented by a continuous distribution of infinitesimal dislocations with density $\rho(x)$.

$$\rho(x) = \frac{dS(x)}{dx} \tag{7}$$

The Burgers vector b is the sum of those of all these infinitesimal dislocations leading to the following normalisation condition:

$$\int_{-\infty}^{+\infty} \rho(x)dx = \int_{-\infty}^{+\infty} \frac{dS(x)}{dx}dx = b \tag{8}$$

The restoring force F acting between atoms on either sides of the interface is balanced by the resultant stress of the distribution of infinitesimal dislocations. This leads to the so-called PN equation:

$$\frac{K}{2\pi}\int_{-\infty}^{+\infty} \frac{1}{x-x'}\left[\frac{dS(x')}{dx'}\right]dx' = \frac{K}{2\pi}\int_{-\infty}^{+\infty} \frac{\rho(x')}{x-x'}dx' = F(S(x)) \tag{9}$$

where K is the energy coefficient introduced above which depends on the dislocation character θ (equation 5). In the original model, the PN equation was solved by introducing a sinusoidal restoring force yielding a well known analytical solution. However, Joos *et al.* (1994) pointed out that, in a real crystal, the restoring force could be quite different from sinusoidal. Christian & Vitek (1970) have suggested that the GSF could be used to calculate the restoring force. Indeed, the GSF is usually not stable and must be balanced by a restoring force $F(S) = -\frac{\partial\gamma}{\partial S}$ (see equation (6)), which can be used to solve the PN equation.

In this paper, we follow the methodology proposed by Joos *et al.* (1994) and already applied with success in several cases (*e.g.* Hartford *et al.*, 1998). The disregistry distribution in the dislocation core $S(x)$ was obtained by searching for a solution in the form:

$$S(x) = \frac{b}{2} + \frac{b}{\pi}\sum_{i=1}^{N}\alpha_i \cdot \arctan\frac{x-x_i}{c_i} \tag{10}$$

where α_i, x_i and c_i are variational constants. Using the previous form of $S(x)$, the infinitesimal dislocation density $\rho(x)$ is

$$\rho(x) = \frac{dS(x)}{dx} = \frac{b}{\pi}\sum_{i=1}^{N}\alpha_i \frac{c_i}{(x-x_i)^2 + c_i^2} \tag{11}$$

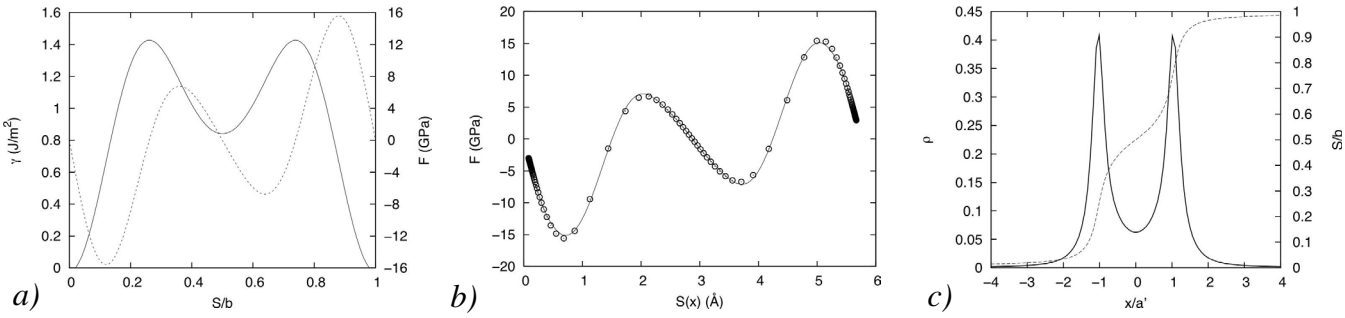

Fig. 8. Example of a determination of the dislocation density ρ and disregistry S for a ½<110>{111} screw dislocations calculated at 0 GPa. (a) GSF and derived restoring force F (dashed line) plotted as a function of S/b (b) Restoring force F (from *ab initio* calculations) and fitted solution F^{PN} as a function of disregistry S (equation 10). The restoring force F from *ab initio* calculations are represented by the open circles and the curve represents the solution of the fit F^{PN} (equation 12). (c) Disregistry S (dashed line) and dislocation density ρ plotted against the distance of the dislocation core.

As the disregistry $S(x)$ and the density $\rho(x)$ must be solution of the normalisation condition, the α_i are constrained by $\sum_{i=1}^{N}\alpha_i = 1$. Then, the previous disregistry function is used to solve the PN equation. Substituting the disregistry into the left-hand side of the PN equation, gives the restoring force

$$F^{PN}(x) = \frac{Kb}{2\pi}\sum_{i=1}^{N}\alpha_i \cdot \frac{x - x_i}{(x-x_i)^2 + c_i^2} \qquad (12)$$

The variational constants α_i, x_i and c_i are obtained from a least square minimisation of the difference between F^{PN} and the restoring force F from our *ab initio* calculations. Practically, the restoring force is obtained by derivating the GSF calculated *ab initio*. It is then fitted by a sine series. N = 3 (equation 10) is sufficient to describe the disregistry $S(x)$ of a simple (*i.e.* with one maximum only) energy barrier whereas barriers with a camel hump requires more terms: we use N = 6. An example of calculation for a screw dislocation of the system ½<110>{111} is shown on Fig. 8. Figure 8b shows the adjustment of F^{PN} on the restoring force F derived from the GSF (Fig. 8a). The disregistry $S(x)$ and the corresponding dislocation density $\rho(x)$ are presented on Fig. 8c.

Following this method, the Peierls model has been applied to calculate the edge and screw dislocations belonging to the three slip systems ½<110>{001}, ½<110>{110}

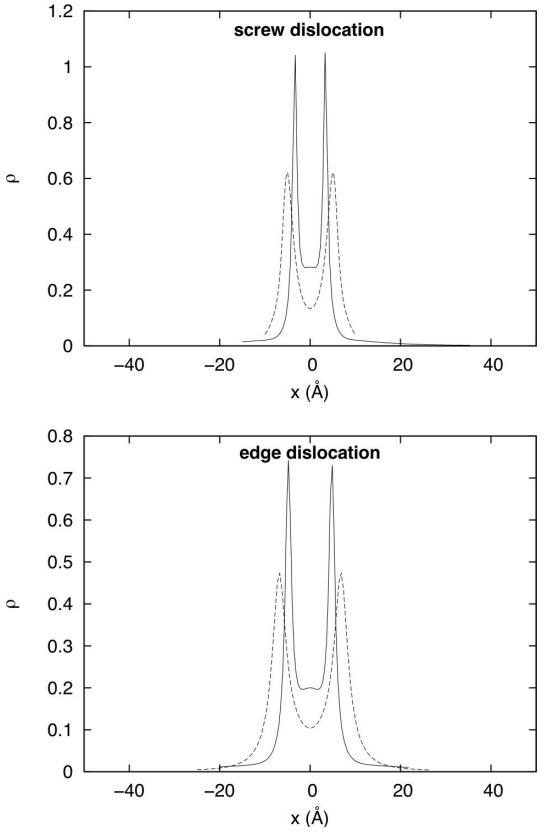

Fig. 9. ½<110>{100} slip system. Infinitesimal dislocation density distributions ρ corresponding to screw and edge dislocations at 0 (dashed line) and 20 GPa.

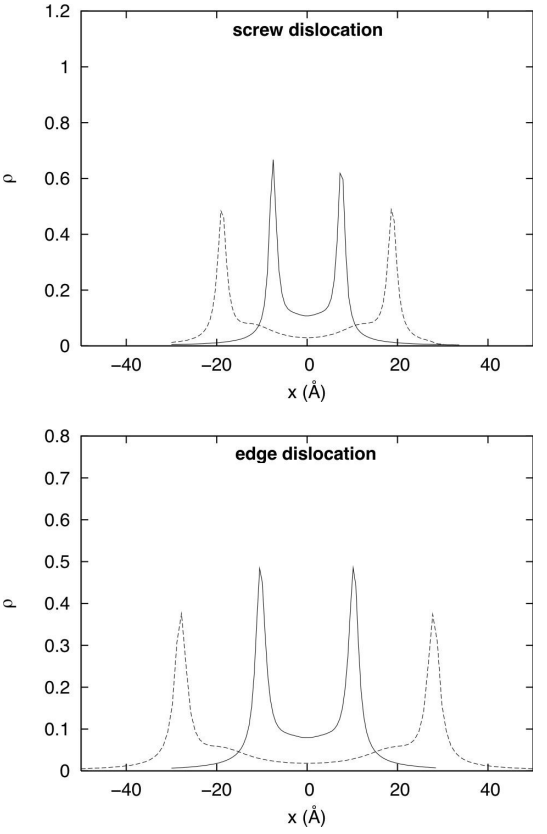

Fig. 10. Same as Fig. 9 for ½<110>{110} slip system.

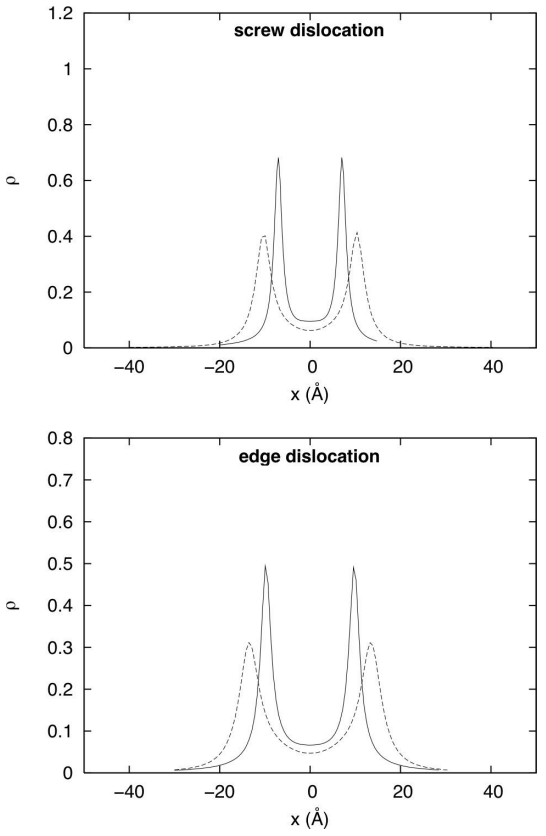

Fig. 11. Same as Fig. 9 for ½<110>{111} slip system.

and ½<110>{111}. The results are presented in Fig. 9, 10 and 11 with the numerical values being given in Tables 2 and 3. The dislocation cores are always found to be significantly spread in the glide plane. The dislocation density functions exhibit two maxima. Camel-hump GSF correspond therefore to a tendency of the dislocation core to dissociate. The dislocation core width ξ is defined as the distance between the two peaks of the density function. At 0 GPa, core spreading is maximum in the {110} planes and minimum in the {100} planes. Pressure is found to have a significant effect on the dislocation core geometries. Application of a 20 GPa pressure results in a more compact dislocation core. Dislocations in {110} and {111} exhibit very comparable dislocation cores at 20 GPa.

Finally, the PN model can be used to calculate the Peierls energy and the stress (called the Peierls stress) required to overcome this energy barrier. Lattice discretisation must be re-introduced at this point as previously the crystal was considered as an elastic continuum medium. Let us consider that in the perfect crystal the distance between planes in the *x* direction is *a'*. The misfit energy can be considered as the sum of misfit energies between pairs of atomic planes and can be written as

$$W(u) = \sum_{m=-\infty}^{+\infty} \gamma(S(ma' - u)) \cdot a' \qquad (13)$$

The Peierls stress is given by:

$$\sigma_P = max\left\{\frac{1}{b}\frac{dW(u)}{du}\right\} \qquad (14)$$

Table 2. Parameters for the PN model for ½<110> screw dislocations. The energy coefficient K (equation 5) and *a'* (periodicity of the Peierls energy W) are input of the PN model. The width of dislocation distribution ξ is obtained as the distance separating the two maximum of the dislocation density function ρ. ΔW and σ_p are respectively the height of the Peierls energy barrier and the Peierls stress needed to overcome this barrier.

Pressure (GPa)	Slip plane	K(0) (GPa)	*a'* (Å)	ξ (Å)	ΔW (eV/Å)	σ_p (GPa)
0	{001}	117	a $\sqrt{2}$/2	10	0.29	6
	{110}		a	37	0.67	11
	{111}		a $\sqrt{6}$/4	20	0.21	4
20	{001}	127	a $\sqrt{2}$/2	6	1.02	34
	{110}		a	15	0.65	10
	{111}		a $\sqrt{6}$/4	14	0.61	14

Table 3. Parameters for the PN model for ½<110> edge dislocations. Parameters are defined as in Table 2.

Pressure (GPa)	Slip plane	K(90) (GPa)	*a'* (Å)	ξ (Å)	ΔW (eV/Å)	σ_p (GPa)
0	{001}	158	a $\sqrt{2}$/2	13	0.32	6
	{110}	150		55	0.21	4
	{111}	154		26	0.09	1.5
20	{001}	177	a $\sqrt{2}$/2	9	0.37	12
	{110}	174		20	0.18	3.5
	{111}	176		19	0.19	5.5

The results of Peierls stresses calculations are presented in Tables 2 and 3 for both screw and edge dislocations. Pressure is found to increase the Peierls stress of dislocations gliding in {100} and {111}. Dislocations gliding in {110} do not present a strong sensitivity to pressure. At 20 GPa, Peierls stresses determined for edge or screw dislocations confirm the results of ISS that suggest glide on {110} and {111} planes is easier than on {100} planes.

6. Prediction of easy slip systems in ringwoodite

A few criteria are usually proposed to predict or account for the choice of the slip systems in crystals (Cordier, 2002):

- Burgers vectors are chosen among the shortest lattice repeats
- Glide planes are chosen among close-packed planes
- The slip plane corresponds to the dissociation plane of the dislocations
- Easy slip systems correspond to minimum values of «b/d_{hkl}» (Chalmers-Martius criterion (Chalmers & Martius, 1952), where b is the Burgers vector magnitude and d_{hkl} the interplanar spacing of the slip plane).

Selecting the smallest Burgers vectors is a criterion of minimum dislocation energy. It is based on the idea that an easy slip system is a slip system where the energy increase yielded by the multiplication of dislocations required for maintaining plastic deformation is smallest. We have calculated the elastic energies associated with several slip systems and shown that, in agreement with the first rule listed

above, ½<110> slip is more likely than <100> slip. We have seen that following crystal chemistry arguments and recent calculations of Durinck *et al.* (2005), the criterion of „close-packed planes" must be replaced in silicates by the choice of planes that do not cut strong Si-O bonds. The weak elastic anisotropy of ringwoodite does not allow us to distinguish between the possible slip planes which satisfy this requirement: {001}, {110} and {111}.

Our calculations of GSF bring further information on the possibility of shearing the ringwoodite structure. The occurrence of <100> slip is ruled out by strong atomic impingements. Rigid body plastic shear is intrinsically easier in {110} and {111}. Plastic shear on {001} seems already most difficult at this stage. The Chalmers-Martius criterion assesses the easiness of slip from the Peierls-Nabarro model in its most simple form (sine profile of the potential). The search for possible dissociation planes can be assisted by the GSF calculations. The existence of a minimum of the GSF curves suggests a possible dissociation. This has been confirmed by the Peierls models of the dislocation cores presented in section 5. Once again, glide is suggested to be easier on {110} and {111} by this approach as a tendency for core spreading is usually related to a greater mobility. It must be underlined that the calculations reported here represent a first approach and do not pretend to give a definite view of the dislocation core structure in ringwoodite. In particular, it must be remembered that the Peierls model considers planar cores only, which represent a strong assumption. The strongest tendency for core spreading in {110} and {111} is however an important information. The calculation of the Peierls stresses not only gives more realistic values than ISS, it also allows us to account for the influence of the core geometry (spreading). As both ISS and core spreading lead to the same conclusion, it is not surprising that the Peierls stresses provide additional support. All together, our calculations suggest that at 20 GPa, the easy slip systems of ringwoodite are ½<110>{110} and ½<110>{111}. It must be noted that those slip systems exhibit a very different evolution with pressure. ½<110>{110} softens slightly while ½<110>{111} hardens significantly with pressure. Our calculations compare very well with recent *in situ* stress measurements from Nishiyama *et al.* (2005) considering that their experiments are dominated by ½<110>{111} slip as shown by Wenk *et al.* (2005). Compared to previous experiments in diamond cells, the measurements of Nishiyama *et al.* (2005) allows the distinction of the actual influence of pressure on plastic shear by removing the strain-hardening contribution. Their stress values compare well with our Peierls stresses, and moreover the pressure evolution of stress reported by Nishiyama *et al.* (2005) is in good agreement with their conclusions of dominant ½<110>{111}.

7. From single crystals to polycrystals

In Fig. 12, we show CPO developed in an aggregate containing one thousand, initially spherical and randomly oriented, ringwoodite grains deformed in simple shear after an

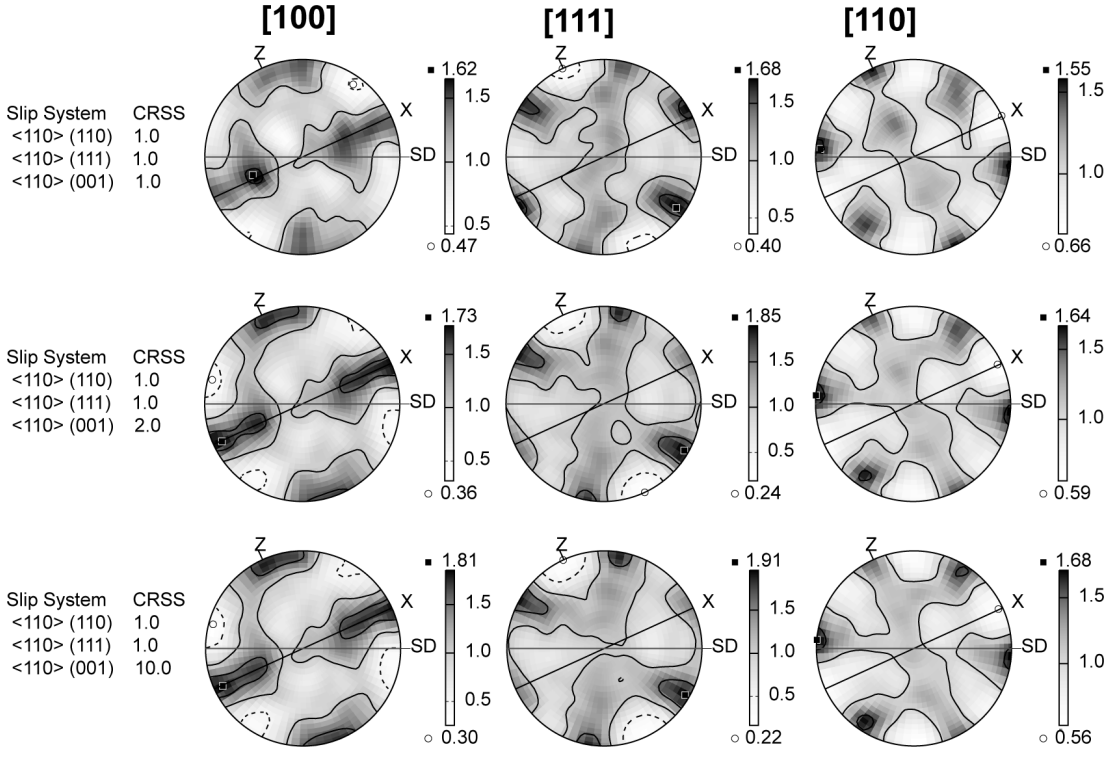

Fig. 12. Ringwoodite crystal preferred orientations predicted by VPSC models at an equivalent strain of 1 (shear strain of 1.73). Critical resolved shear stresses (CRSS) for the 3 slips systems used in the models are displayed to the left of each pole figure. Lower hemisphere equal-area projections, contours at intervals of 0.5 multiple of a uniform distribution, 1000 grains. Dextral shear; SD = shear direction, NSP = normal to the shear plane, which is marked by the horizontal line. Black line marks the foliation (main flattening plane, which normal is Z). X = lineation (main stretching direction).

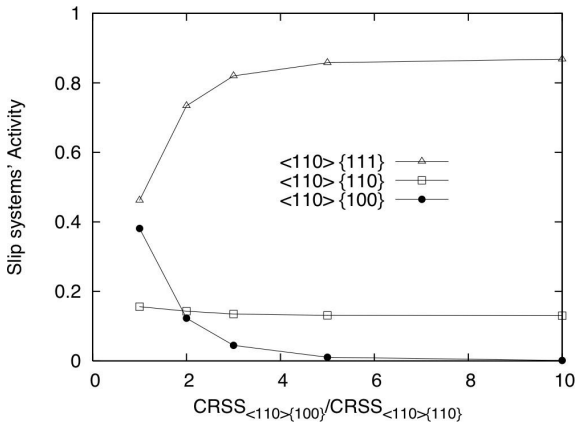

Fig. 13. Slip systems activity at an equivalent strain of 1 as a function of relative strength of {100} slip relative to {110} and {111} in the simple shear VPSC simulations. The activity of a slip system is calculated by averaging over all grains the contribution of this slip system to the local strain rate.

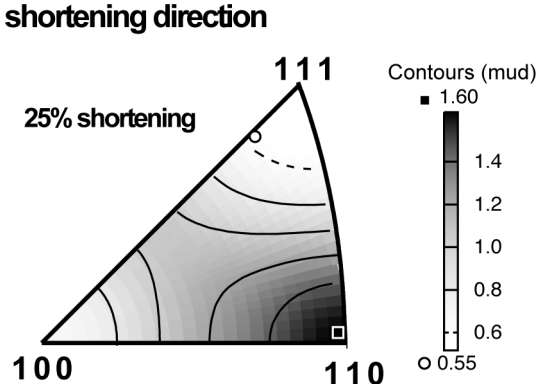

Fig. 14. Inverse pole figure showing the orientation of the shortening direction relative to the ringwoodite crystal axes predicted by VPSC models with critical resolved shear stresses (CRSS) for slip on {110}, {111}, and {100} defined as $CRSS_{\{110\}} = CRSS_{\{111\}} = 1/2\ CRSS_{\{100\}}$, after an axial shortening of 25%. Contours at intervals of 0.2 multiple of a uniform distribution, 1000 grains.

equivalent strain of 1, which corresponds to a dextral simple shear strain of 1.73. The models which are presented involve easy slip along ½<110> on {110} and {111}, *i.e.*, $CRSS_{\{110\}} = CRSS_{\{111\}} = 1$, and increasingly harder slip on {100}, *i.e.*, $CRSS_{\{100\}} = 1$, 2, or 10 and a rate sensitivity, n = 3. Ringwoodite CPO are well developed, but weak (maximum concentrations are always below 2 multiples of an uniform distribution). The CPO are almost insensitive to the variation of CRSS for {100} slip. <100> axes tend to align either within or normal to the foliation (main flattening plane), with a weak maximum close to the lineation (main stretching direction) in those models in which slip on {100} planes are hindered. <111> and <110> axes display both a rough 6-fold distribution with a symmetry axis normal to the shear plane. However, <110> displays a maximum close to the shear direction and some dispersion normal to the lineation or within the shear plane, whereas <111> shows two symmetric maxima at *ca.* 30° to the shear direction and a girdle distribution in a plane at high angle to the shear direction. Once formed, these CPO evolve slowly with increasing strain; CPO modelled for an equivalent strain of 5 show patterns and intensities (maximum concentrations of <100>, <110>, and <111> are 1.7, 1.95 and 1.8 multiples of an uniform density, respectively) similar to those observed after an equivalent strain of 1. Results for models with n = 5 show similar patterns, but stronger concentrations (maximum concentrations of <100>, <110>, and <111> are 1.97, 2.69, and 2.73 multiples of an uniform density, respectively for a model with $CRSS_{\{110\}} = CRSS_{\{111\}} = 1/2\ CRSS_{\{100\}}$ at an equivalent strain of 1). In all cases, slip on {111} dominates the plasticity of the aggregate (Fig. 13). The higher activity of {111} systems results from geometrical constraints. Indeed, in a cubic mineral, this mode is composed by 12 systems whereas {110} and {100} modes are composed by 6 systems each.

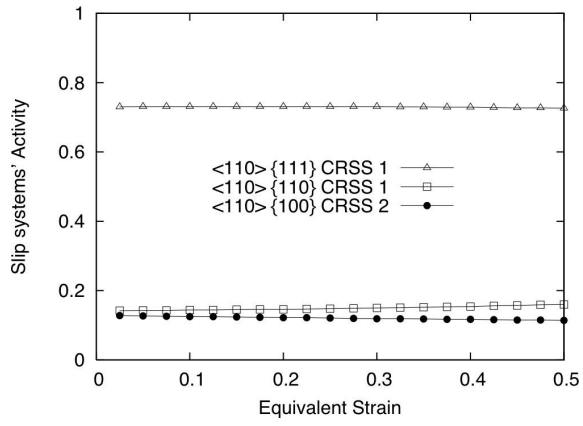

Fig. 15. Slip systems activity as a function of strain in an axial compression VPSC simulation. The activity of a slip system is calculated by averaging over all grains the contribution of this slip system to the local strain rate.

CPO formed in axial compression models in which $CRSS_{\{110\}} = CRSS_{\{111\}} = CRSS_{\{100\}}$ or $CRSS_{\{110\}} = CRSS_{\{111\}} = 1/2\ CRSS_{\{100\}}$ reproduce the pattern observed in room temperature compression experiments in a diamond anvil cell (Wenk *et al.*, 2004) and in a D-DIA (Wenk *et al.*, 2005). {110} planes tend to orient normal to the compression direction (Fig. 14), because deformation in these models is essentially accommodated by slip on {111} planes (Fig. 15). The orientation of {110} normal to compression direction in these models results therefore from a geometrical effect associated with the simultaneous activation of various ½<110>{111} systems. Similar geometrical effects have also been observed to occur in other minerals, like clinopyroxenes (Bascou *et al.*, 2002). These results highlight that the interpretation of slip system activity from the analysis of measured CPO is not straightforward when deformation is essentially accommodated by prismatic or pyramidal slip systems, emphasising the importance of TEM data and of forward simulations, like the ones presented here, in the evaluation of the slip systems' activity.

8. Concluding remarks

It is now possible to use first-principle calculations to assess the resistance of minerals to plastic shear from GSF calcula-

tions. We show in this study that GSF can be used as input data to infer dislocations properties from the Peierls model. This approach has been used here for the first time to predict the plastic properties of a mineral under high-pressure conditions. Our calculations suggest that ½<110>{110} and ½<110>{111} are the easiest slip systems in ringwoodite at 20 GPa. VPSC calculations of CPO using these data are shown to account satisfactorily for experimental data obtained at room temperature in diamond anvil cell and D-DIA experiments. The approach illustrated in the present work opens a new field in the study of plasticity of minerals under extreme pressure conditions. The next step will be of course to incorporate the influence of temperature on plastic slip. Our approach cannot predict if a change of slip system occurs with temperature. We observe that our predictions are in agreement with the HP-HT deformation experiments of Thurel (2001), but not with those of Karato *et al.* (1998) who reported slip on {100}. It is not clear whether the discrepancy between those results is due to a sampling problem or if other parameters (differences in the iron content for instance) are involved. In any case, the deformation of ringwoodite seems to produce relatively weak crystal preferred orientations. Given the modest elastic anisotropy of ringwoodite at pressure and temperature of the transition zone (Mainprice *et al.*, 2000) and the weak crystal preferred orientations it develops, it is unlikely that plastic deformation of ringwoodite generates a marked seismic anisotropy in the transition zone between 520 and 670 km depth.

Acknowledgements: We acknowledge the contribution of C. Terrier and F. Vasconcelos for the calculations and thank J. Douin (CEMES, Toulouse) for helpful discussions. Thoughtful comments from the associate editor, H.-R. Wenk and an anonymous referee helped us in improving the paper. This work was supported by CNRS-INSU under the DyETI programme. Computational resources were provided by IDRIS (project # 031685) and CRI-USTL supported by the Fonds Européens de Développement Régional.

References

Barron, T.H.K. & Klein, M.L. (1965): Second-order elastic constants of a solid under stress. *Proc. Phys. Soc.*, **85**, 523–531.

Bascou, J., Tommasi, A., Mainprice, D. (2002): Plastic deformation and development of clinopyroxene lattice preferred orientations in eclogites. *J. Struct. Geol.*, **24**, 1357–1368.

Chalmers, B. & Martius, U.M. (1952): Slip planes and the energy of dislocations. *Proc. R. Soc. London A*, **213**, 175–185.

Christian , J.W. & Vitek, V. (1970): Dislocations and Stacking Faults. *Rep. Prog. Phys.*, **33**.

Clatterbuck, D.M., Krenn, C.R., Cohen, M.L., Morris Jr., J.W. (2003): Phonon instabilities and the ideal strength of aluminum. *Phys. Rev. B Condensed Matter*, **91**, 5501–5504.

Cordier, P. (2002): Dislocation and slip systems of mantle minerals. *in* „Plastic deformation of minerals and rocks", *Reviews in Mineralogy*, **41**, Mineralogical Society of America ed.

Cordier, P. & Rubie, D.C. (2001): Plastic deformation of minerals under extreme pressure using a multi-anvil apparatus. *Mater. Sci. Eng. A Struct. Mater.*, **309**, 38–43.

Cordier, P., Ungár, T., Zsoldos, L., Tichy, G. (2004): Dislocation creep in $MgSiO_3$ Perovskite at conditions of the Earth's uppermost lower mantle. *Nature*, **428**, 837–840.

de Koning, M., Antonelli, A., Bazant, M.Z., Kaxiras, E., Justo, J.F. (1998): Finite-temperature molecular-dynamics study of unstable stacking fault free energies in silicon. *Phys. Rev. B Condensed Matter*, **58**, 12555–12558.

Domain, C., Besson, R., Legris, A. (2004): Atomic-scale ab initio study of the Zr-H system: II. Interaction of H with plane defects and mechanical properties. *Acta Materialia*, **52**, 1495–1502.

Douin, J. (1987): Structure fine des dislocations et plasticité dans Ni_3Al. PhD Thesis, University of Poitiers, France.

Douin, J., Veyssière, P., Beauchamp, P. (1986): Dislocation line stability in Ni_3Al. *Philos. Mag. A*, **54**, 375–393.

Durinck, J., Legris, A., Cordier, P. (2005): Influence of crystal chemistry on ideal plastic shear anisotropy in forsterite: first principle calculations. *Am. Mineral.*, **90**, 1072–1077.

Hartford, J., von Sydow, B., Wahnström, G., Lundqvist, B.I. (1998): Peierls barrier and stresses for edge dislocations in Pd and Al calculated from first principles. *Phys. Rev. B*, **58**, 2487–2496.

Hirth, J.P. & Lothe, J. (1982): Theory of dislocations. Wiley-Interscience Publication.

Irifune, T. & Ringwood, A.E. (1987): Phase transformations in a harzburgite composition to 26 GPa: implications for dynamical behavior of the subducting slab. *Earth Planet. Sci. Lett.*, **86**, 365–376.

Joos, B., Ren, Q., Duesbery, M.S. (1994): Peierls-Nabarro model of dislocations in silicon with generalized stacking-fault restoring forces. *Phys. Rev. B*, **50**, 5890–5898.

Karato, S.I., Dupas-Bruzek, C., Rubie, D.C. (1998): Plastic deformation of silicate spinel under the transition-zone conditions of the Earth's mantle. *Nature*, **395**, 266–269.

Kavner, A. & Duffy, T.S. (2001): Strength and elasticity of ringwoodite at upper mantle pressures. *Geophys. Res. Lett.*, **28**, 2691–2694.

Kaxiras, E. & Duesbery, M.S. (1993): Free energies of generalyzed stacking faults in Si and implications for the brittle-ductile transition. *Phys. Rev. Lett.*, **70**, 3752–3755.

Kiefer, B., Stixrude, L., Wentzcovitch, R.M. (1997): Calculated elastic constants and anisotropy of Mg_2SiO_4 spinel at high pressure. *Geophys. Res. Lett.*, **24**, 2841–2844.

Krenn, C.R., Roundy, D., Morris Jr., J.W., Cohen, M.L. (2001): the nonlinear elastic behavior and ideal shear strength of Al and Cu. *Materials Sci. Eng. A*, **317**, 44–48.

Kresse, G. & Furthmüller, J. (1996a): Efficiency of ab-initio total energy calculations for metals and semiconductors using a plane-wave basis set. *Comput. Mat. Sci.*, **6**, 15–50.

–,– (1996b): Efficient iterative schemes for ab initio total-energy calculations using a plane-wave basis set. *Phys. Rev. B*, **54**, 11169.

Kresse, G. & Hafner, J. (1993): Ab initio molecular dynamics for liquid metals. *Phys. Rev. B*, **47**, 558.

–,– (1994): Norm-conserving and ultrasoft pseudopotentials for first-row and transition elements. *J. Phys.: Condens. Mat.*, **6**, 8245.

Lebensohn, R.A. & Tomé, C.N. (1993): A self-consistent anisotropic approach for the simulation of plastic deformation and texture development of polycrystal: application to zirconium alloys. *Acta Metall. Mater.*, **41**, 2611–2624.

Lebensohn, R.A., Dawson, P.R., Kern, H.M., Wenk, H.R. (2003): Heterogeneous deformation and texture development in halite polycrystals: comparison of different modeling approaches and experimental data. *Tectonophysics*, **370**, 287–311.

Logé, R.E., Signorelli, J.W., Chastel, Y.B., Perrin, M.Y., Lebensohn, R.A. (2000): Sensitivity of alpha-Zy4 high-temperature deformation textures to beta-quenched precipitate structure and to recrystallization: application to hot extrusion. *Acta Mater.*, **48**, 3917–3930.

Luo, W., Roundy, D., Cohen, M.L., Morris Jr., J.W. (2002): Ideal strength of bcc molybdenum and niobium. *Phys. Rev. B*, **B66**, 1–7.

Madon, M. & Poirier, J.P. (1983): Transmission electron microscope observation of a, b and g (Mg, Fe)$_2$SiO$_4$ in shocked meteorites: planar defects and polymorphic transitions. *Phys. Earth Planet. Int.*, **33**, 31–44.

Mainprice, D., Barruol, G., Ben Ismaïl, W. (2000): The seismic anisotropy of the Earth's mantle: from single crystal to polycrystal. *in* „Earth deep interior: mineral physics and tomography from the atomic scale to the global scale", S.I. Karato, Ed. American Geophysical Union, Washington, D.C., 237–264.

Mainprice, D., Bascou, J., Cordier, P., Tommasi, A. (2004): Crystal preferred orientations of garnet: comparisons between numerical simulations and electron back-scattered diffraction (EBSD) measurements in naturally deformed eclogites. *J. Struct. Geol.*, **26**, 2089–2102.

Medvedeva, N.I., Mryasov, O.N., Gornostyrev, Y.N., Novikov, D.L., Freeman, A.J. (1996): First-principles total-energy calculations for planar shear and cleavage decohesion processes in B2-ordered NiAl and FeAl. *Phys. Rev. B*, **54**, 13506–13514.

Miranda, C.R. & Scandolo, S. (2005): Computational materials science meets geophysics: dislocations and slip planes of MgO. *Comp. Phys. Comm.*, **169**, 24–27.

Mitchell, T.E. (1999): Dislocations and mechanical properties of MgO-Al$_2$O$_3$ spinel single crystals. *J. Amer. Ceram. Soc.*, **82**, 3305–3316.

Molinari, A., Canova, G.R., Azhy, S. (1987): A self-consistent approach of the large deformation crystal polycrystal viscoplasticity. *Acta Metall.*, **35**, 2983–2994.

Monkhorst, H.J. & Pack, J.D. (1976): Special points for Brillouin-zone integrations. *Phys. Rev. B*, **23**, 5048–5192.

Mryasov, O.N., Gornostyrev, Y.N., Freeman, A.J. (1998): Generalized stacking-fault energetics and dislocation properties: compact versus spread unit-dislocation structures in TiAl and CuAu. *Phys. Rev. B Condensed Matter*, **58**, 11927–11932.

Nishiyama, N., Wang, Y., Uchida, T., Rivers, M.L., Sutton, S.R. (2005): Pressure and strain dependence of the strength of sintered polycrystalline Mg$_2$SiO$_4$ ringwoodite. *Geophys. Res. Lett.*, **32**, L04307.

Ogata, S., Li, J., Yip, S. (2002): Ideal pure shear strength of aluminum and copper. *Science*, **298**, 807–811.

Paxton, A.T., Gumbsch, P., Methfessel, M. (1991): A quantum mechanical calculation of the theoretical strength of metals. *Philos. Mag. Lett.*, **63**, 267–274.

Perdew, J.P. & Wang, Y. (1992): Accurate and simple analytic representation of the electron-gas correlation energy. *Phys. Rev. B*, **45**, 13244–13249.

Putnis, A. & Price, G.D. (1979): High pressure (Mg,Fe)$_2$SiO$_4$ phases in the Tenham chondritic meteorite. *Nature*, **280**, 217–218.

Roundy, D., Krenn, C.R., Cohen, M.L., Morris Jr., J.W. (1999): Ideal shear strengths of fcc aluminum and copper. *Phys. Rev. Lett.*, **82**, 2713–2716.

Roundy, D., Krenn, C.R., Cohen, M.L., Morris Jr., J.W. (2001): The ideal strength of tungsten. *Philos. Mag. A*, **81**, 1725–1747.

Rubie, D.C. & Brearley, A.J. (1990): Mechanism of the g-b-phase transformation of Mg$_2$SiO$_4$ at high pressure and temperature. *Nature*, **348**, 628–631.

–,– (1994): Phase transitions between beta and gamma (Mg,Fe)$_2$SiO$_4$ in the Earth's mantle: Mechanisms ans rheological implications. *Science*, **264**, 1445–1448.

Sinogeikin, S.V., Bass, J.D., Katsura, T. (2001): Single-crystal elasticity of g-(Mg$_{0.91}$Fe$_{0.09}$)$_2$Si0$_4$ to high pressures and to high temperatures. *Geophys. Res. Lett.*, **28**, 4335–4338.

Söderlind, P. & Moriarty, J.A. (1998): First-principles theory of Ta up to 10 Mbar pressure: Structural and mechanical properties. *Phys. Rev. B*, **57**, 10340–10350.

Sun, Y. & Kaxiras, E. (1997): Slip energy barrier in aluminum and implications for ductile-brittle behaviour. *Philos. Mag. A*, **75**, 1117–1127.

Thurel, E. (2001): Etude par microscopie électronique en transmission des mécanismes de déformation de la wadleyite et de la ringwoodite. PhD Thesis, University of Lille, France.

Tomé, C.N. & Canova, G. (2000): Self-consistent modelling of heterogeneous plasticity. *in* „Texture and Anisotropy – Preferred Orientations in Polycrystals and their effects on Materials Properties", U.F. Kocks, C.N. Tomé, H.R. Wenk, Eds. Cambridge University Press, Cambridge, 466–509.

Tomé, C.N., Wenk, H.-R., Canova, G., Kocks, U.F. (1991): Simulations of texture development in calcite: comparison of polycrystal plasticity theories. *J. Geophys. Res.*, **96**, 11865–11875.

Tommasi, A., Mainprice, D., Canova, G., Chastel, Y. (2000): Viscoplastic self-consistent and equilibrium-based modeling of olivine lattice preferred orientations: Implications for the upper mantle seismic anisotropy. *J. Geophys. Res. Solid Earth*, **105**, 7893–7908.

Tommasi, A., Cordier, P., Mainprice, D., Couvy, H., Thoraval, C. (2004): Strain-induced seismic anisotropy of wadsleyite polycrystal: constraints on flow patterns in the mantle transition zone. *J. Geophys. Res.*, **109**, B12405.

Vanderbilt, D. (1990): Soft self-consistent pseudopotentials in a generalized eigenvalue formalism. *Phys. Rev. B*, **41**, 7892–7895.

Vaughan, P.J. & Kohlstedt, D.L. (1981): Cation stacking faults in magnesium germanate spinel. *Phys. Chem. Minerals*, **7**, 241–245.

Vítek, V. (1968): Intrinsic stacking faults in body-centered cubic crystals. *Phil. Mag. A*, **18**, 773–786.

– (1974): Theory of the core structures of dislocations in body-centered-cubic metals. *Crystal Lattice Defects*, **5**, 1–34.

Walker, A.M. (2004): Computational studies of point defects and dislocations in forsterite (Mg$_2$SiO$_4$) and some implications for the rheology of mantle olivine. PhD Thesis, University College, London, U.K.

Wang, Y., Durham, W.B., Getting, I., Weidner, D.J. (2003): The deformation-DIA: a new apparatus for high-temperature triaxial deformation to pressures up to 15 GPa. *Rev. Sci. Instrum.*, **74**, 3002–3011.

Wenk, H.R., Lonardelli, I., Pehl, J., Devine, J., Prakapenka, V., Shen, G., Mao, H.-K. (2004): In situ observation of texture development in olivine, ringwoodite, magnesiowüstite and silicate perovskite. *Earth Planet. Sci. Lett.*, **226**, 507–519.

Wenk, H.R., Bennet, K., Canova, G.R., Molinari, A. (1991) Modelling plastic deformation of peridotite with the self-consistent theory. *J. Geophys. Res.*, **96**, 8337–8349.

Wenk, H.R., Ischia, G., Nishiyama, N., Wang, Y., Uchida, T. (2005): Texture development and deformation mechanisms in ringwoodite. *Phys. Earth Planet. Int.*, **152**, 191–199.

Xu, W. & Moriarty, J.A. (1996): Atomistic simulation of ideal shear strength, point defects, and screw dislocations in bcc transition metals: Mo as a prototype. *Phys. Rev. B*, **54**, 6941–6951.

Xu, Y.Q., Weidner, D.J., Chen, J.H., Vaughan, M.T., Wang, Y.B., Uchida, T. (2003): Flow-law for ringwoodite at subduction zone conditions. *Phys. Earth Planet. Interiors*, **136**, 3–9.

Yamazaki, D. & Karato, S. (2001): High-pressure rotational deformation apparatus to 15 GPa. *Rev. Sci. Instr.*, **72**, 4207–4211.

Received 20 July 2005
Modified version received 17 October 2005
Accepted 14 November 2005